An Introduction to Topological Materials: SSH Model, Graphene, and the Haldane Model

Katsunori Kubo
Advanced Science Research Center, Japan Atomic Energy Agency, Japan

We review three representative models of topological materials: the Su–Schrieffer–Heeger (SSH) model, graphene, and the Haldane model. In this note, we use the term graphene to refer to the tight-binding model with nearest-neighbor hopping on a honeycomb lattice. The SSH model describes a one-dimensional topological insulator. When regarded as a two-dimensional model, it has a point defect of a two-component vector. This point defect underlies the realization of the topological insulator, giving rise to edge states in a system with edges. Graphene is a model of a two-dimensional topological semimetal. As in the SSH model, point defects of a two-component vector appear, leading to the emergence of edge states for systems with edges. By extending graphene, we obtain the Haldane model, a model of a two-dimensional topological insulator. Viewed as a three-dimensional model, it has point defects of a three-component vector. These defects are responsible for the realization of the topological insulator and the appearance of edge states in systems with edges. The topology of these models and their point defects is characterized by the winding number.

SSH Model

Hamiltonian and Energy Bands

The Su–Schrieffer–Heeger (SSH) model is a one-dimensional tight-binding model with alternating hopping amplitudes [1], as illustrated in Fig. 1. When two sites connected by the $(1+\delta)t$ hopping are chosen as a unit cell, the Hamiltonian can

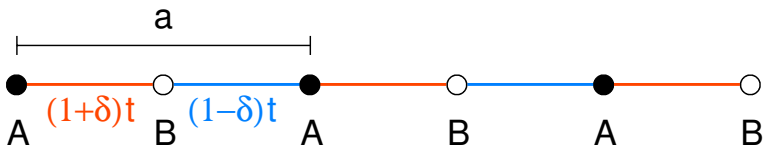

Figure 1: SSH model. a is the lattice constant.

be written as:

$$
\begin{aligned}
H &= t\sum[(1+\delta)c_{rA}^{\dagger}c_{rB} + (1-\delta)c_{rA}^{\dagger}c_{r-aB}] + \text{h.c.} \\
&= t\frac{1}{N}\sum[(1+\delta)e^{-ikr+ik'r} + (1-\delta)e^{-ikr+ik'(r-a)}]c_{kA}^{\dagger}c_{k'B} + \text{h.c.} \\
&= t\sum[(1+\delta) + (1-\delta)e^{-ika}]c_{kA}^{\dagger}c_{kB} + \text{h.c.} \\
&= t\sum\{[(1+\delta) + (1-\delta)e^{-ika}]c_{kA}^{\dagger}c_{kB} + [(1+\delta) + (1-\delta)e^{ika}]c_{kB}^{\dagger}c_{kA}\} \\
&= \sum c_k^{\dagger}[h_x(k)\sigma_x + h_y(k)\sigma_y]c_k.
\end{aligned}
$$

$$
\begin{aligned}
h_x(k) &= (1+\delta) + (1-\delta)\cos(ka), \\
h_y(k) &= (1-\delta)\sin(ka).
\end{aligned}
$$

Here, σ_x and σ_y denote the Pauli matrices, and we define $c_k = (c_{kA}, c_{kB})^{\mathrm{T}}$. The energy eigenvalues are given by $\pm h(k) = \pm|\boldsymbol{h}(k)|$, where $\boldsymbol{h}(k) = \big(h_x(k), k_y(k)\big)$.

The energy bands are shown in Fig. 2. In the following, we consider the half-filled case. The energy gap at wave number k is $2h(k)$; thus, if $h(k) = 0$ at some k, the system is metallic, whereas otherwise it is insulating. The system becomes metallic only when $\delta = 0$, in which case $h(k) = 0$ at $k = \pi/a$. For any nonzero δ, the system is insulating.

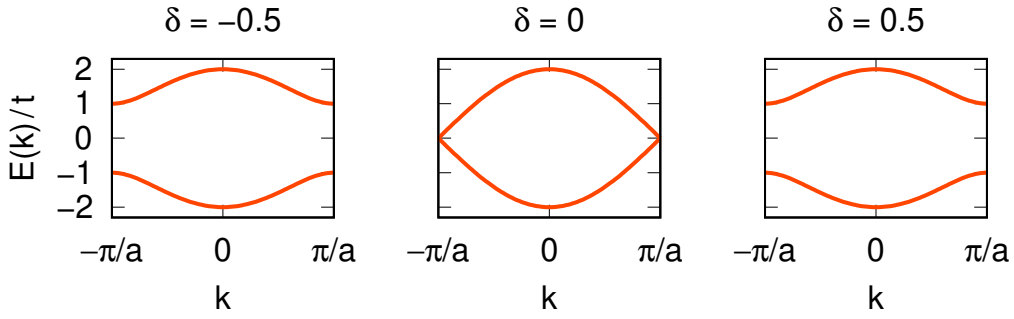

Figure 2: Energy bands of the SSH model.

Winding Number of the Vector $\boldsymbol{h}(k)$

Figure 3 shows the behavior of the vector $\boldsymbol{h}(k)$ as k varies from 0 to $2\pi/a$. For $\delta = -1$, $\boldsymbol{h}(k)$ makes one counterclockwise rotation over this interval. In this case, the system is assigned a winding number $w = 1$. The winding number remains unchanged for all $\delta < 0$. On the other hand, for $\delta > 0$, $\boldsymbol{h}(k)$ does not exhibit such a structure. As k varies from 0 to $2\pi/a$, $\boldsymbol{h}(k)$ does not rotate even once. In this case, the system is assigned a winding number $w = 0$. Since the winding number is an integer, it cannot change continuously. Indeed, at $\delta = 0$, which separates the regions with $w = 1$ and $w = 0$, $\boldsymbol{h}(k) = \boldsymbol{0}$ at $k = \pi/a$, making the winding number undefined. The winding number as a function of δ is shown in Fig. 4. The winding number can also be expressed by the following formula:

$$w = \int_0^{2\pi/a} \frac{dk}{2\pi} \left[\hat{h}_x(k) \frac{d}{dk} \hat{h}_y(k) - \hat{h}_y(k) \frac{d}{dk} \hat{h}_x(k) \right],$$

where $\hat{\boldsymbol{h}}(k) = \boldsymbol{h}(k)/h(k)$.

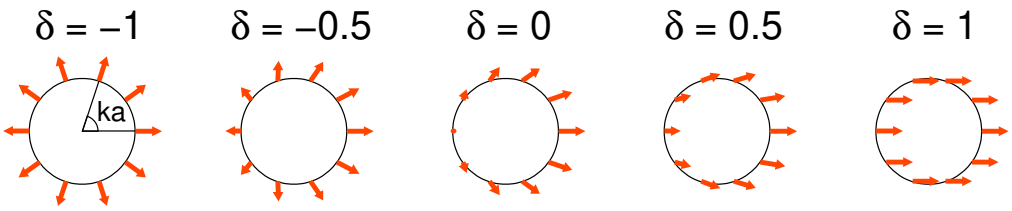

Figure 3: Vector $\boldsymbol{h}(k)$. Each k point ($0 \leq k < 2\pi/a$) corresponds to a point on a circle. $\boldsymbol{h}(k)$ at each k point is illustrated by the arrow.

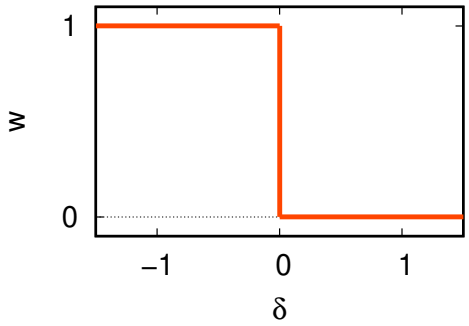

Figure 4: Winding number of the SSH model.

Topological Insulator and Edge States

For $\delta < 0$, the system is an insulator with a topological structure characterized by $w = 1$; such a system is called a topological insulator. In contrast, for $\delta > 0$, the system does not have such a special structure and is referred to as a trivial insulator. Changing the winding number requires passing through the metallic state at $\delta = 0$, where the winding number is undefined. In other words, a transition from a topological insulator to a trivial insulator necessarily passes through a metallic state.

The vacuum can be regarded as a trivial insulator. When a topological insulator has an edge, the system transitions from a topological insulator to a trivial insulator around the edge. Consequently, a metallic region must appear somewhere around the edge. In other words, a metallic state is expected to emerge on the edge of a topological insulator. Figure 5 shows the single-particle energies of a system with edges. Since the wave number is not defined for a finite system, the energies are plotted simply in order from lowest to highest. For a topological insulator with $\delta = -0.5$, metallic states with zero energy indeed appear. These states lie in an energy range where the bulk bands are absent (see Fig. 2), indicating that they exist solely due to the presence of edges; that is, they are localized on the edges. In contrast, for a trivial insulator with $\delta = 0.5$, no such edge states are observed.

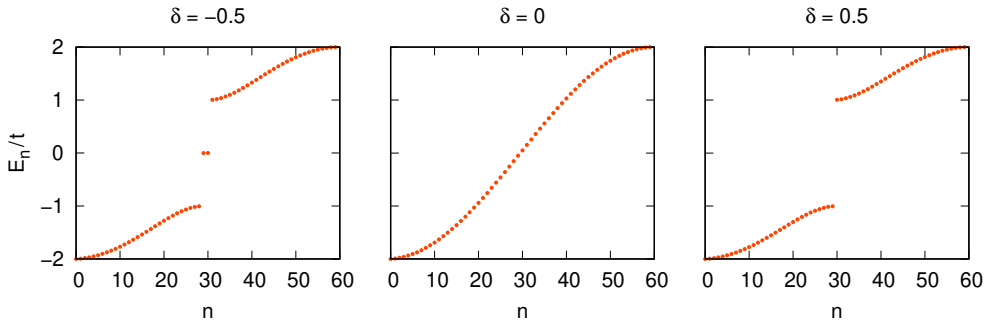

Figure 5: Single-particle energies of the SSH model with finite length $L = 30a$.

Chiral Symmetry and Zero-Energy Eigenstates

In models with hopping only between the A and B sublattices, such as the SSH model, the Hamiltonian can be expressed in the following matrix form:

$$H = \begin{pmatrix} 0 & H_{AB} \\ H_{BA} & 0 \end{pmatrix}.$$

Here, we introduce the following unitary matrix:

$$\Gamma = \begin{pmatrix} I_A & 0 \\ 0 & -I_B \end{pmatrix},$$

where I_A and I_B denote the identity matrices for the A and B sublattices, respectively. This operator Γ anticommutes with the Hamiltonian. When a unitary operator Γ with this property exists, the Hamiltonian is said to have chiral symmetry, and Γ is called the chiral operator. In the present case, Γ is also Hermitian, so that $\Gamma^2 = \Gamma^\dagger\Gamma = I$, where I is the identity matrix. Therefore, the eigenvalues of Γ are $\gamma = \pm 1$. The $\gamma = 1$ states have nonzero amplitude only on the A sublattice, while the $\gamma = -1$ states have nonzero amplitude only on the B sublattice.

When the Hamiltonian H anticommutes with Γ, we can show that H^2 and Γ commute. In other words, H^2 and Γ are simultaneously diagonalizable. Let $|u_0\rangle$ be a zero-eigenvalue state of H^2.

$$\langle u_0|H^\dagger H|u_0\rangle = \langle u_0|H^2|u_0\rangle = 0.$$

Therefore, $H|u_0\rangle = 0$, meaning that $|u_0\rangle$ is a zero-energy eigenstate. Conversely, it is obvious that any zero-energy eigenstate is a zero-eigenvalue state of H^2. From the above, a zero-energy eigenstate can be composed as an eigenstate of the chiral operator [2].

The two zero-energy eigenstates shown in the left panel of Fig. 5 are superpositions of states localized on the left and right edges. For a sufficiently long system, the states localized on the left and right edges can be treated as independent. Consequently, an edge state is an eigenstate of the chiral operator, meaning it has nonzero amplitudes only on a single sublattice. The charge density of the edge states is shown in Fig. 6. The charge density is finite only on the A sublattice on the left edge and the B sublattice on the right edge.

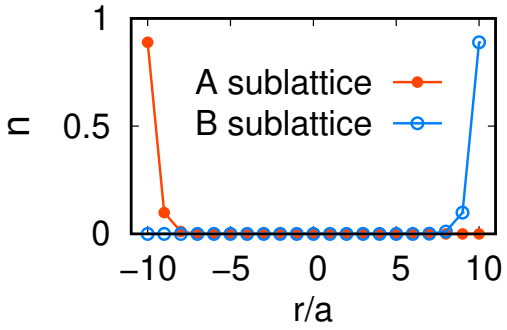

Figure 6: Charge density of the zero-energy eigenstates of the SSH model with finite length $L = 21a$. $\delta = -0.5$. The charge density of the two degenerate states has been summed.

SSH Model as a Two-Dimensional Model

Energy Bands of a System with Finite Width

We have obtained the energy distribution of a system with edges for various values of δ, as shown in Fig. 5. Figure 7 shows the energy distribution as a function of δ. From this figure, we can see at a glance that zero-energy edge states appear in the region of $\delta < 0$, that is, for topological insulators ($w \neq 0$). This figure can also be regarded as the energy bands of a system defined in the two-dimensional space of (δ, r) with finite width $0 \leq r < L$. The system with finite width is a one-dimensional system in the direction along the edges (δ direction).

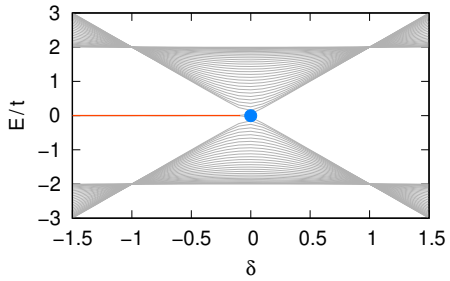

Figure 7: Energy bands as a function of δ of the SSH model. The width of the system is $L = 30a$. The red line is the zero-energy edge state corresponding to $w = 1$. The blue point is the projection of the Dirac point with winding number -1 (see below).

Energy Bands

Considering the above, we can regard the SSH model defined in the two-dimensional wave-number space of (δ, k). Figure 8 shows the energy bands. While the system is not periodic in δ, we plot here in the range of $|\delta| < 1$. The upper and lower bands touch at a point $(\delta, k) = (0, \pi/a)$. This point is called a Dirac point.

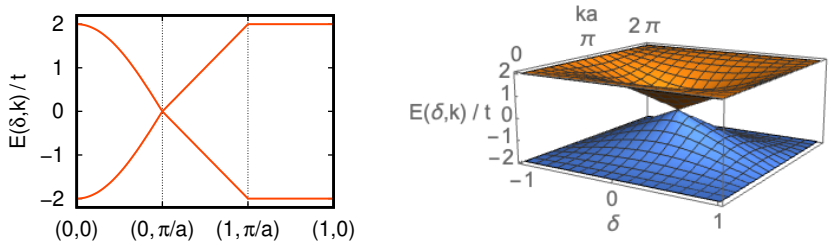

Figure 8: Energy bands as a function of (δ, k) of the SSH model. The left panel shows the energy bands along high-symmetry lines. The right panel shows the energy bands in the entire region within $|\delta| < 1$.

Winding Number of the Vector $\boldsymbol{h}(\boldsymbol{k}_{\mathrm{2D}})$

Figure 9 shows $\hat{\boldsymbol{h}}(k)$ on the δ-k plane. $\hat{\boldsymbol{h}}(k)$ cannot be defined at the Dirac point (point defect), so it is not drawn there. $\hat{\boldsymbol{h}}(k)$ rotates once clockwise along a counterclockwise path encircling the Dirac point. Thus, we can define the winding number of the Dirac point as -1. We also show an example of a vector field with winding number 1 in Fig. 10. Such a point defect of a two-component vector in two-dimensional space is known to be topologically stable (see, for example, Ref. [3]). In other words, this point defect cannot be eliminated by continuously changing $\hat{\boldsymbol{h}}(k)$.

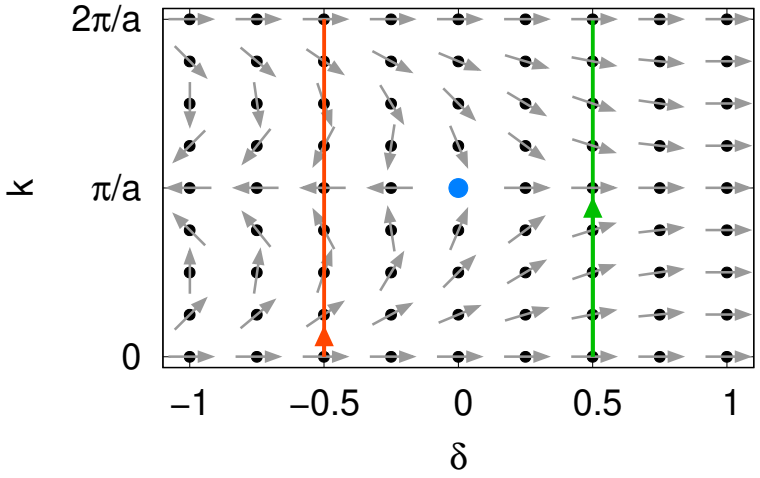

Figure 9: $\hat{\boldsymbol{h}}(k)$ on the δ-k plane of the SSH model. The blue point is the Dirac point with winding number -1. $\hat{\boldsymbol{h}}(k)$ rotates once counterclockwise along the red path and does not rotate even once along the green path.

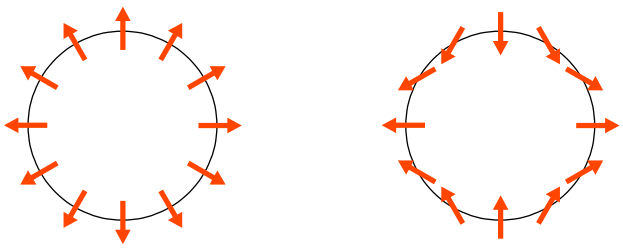

Figure 10: Examples of vector fields with finite winding numbers. Left: winding number 1; Right: winding number -1.

Table 1: Winding number of the SSH model. By increasing δ, the path $0 \leq k < 2\pi/a$ crosses the Dirac point with $w_C = -1$ and the winding number reduces by 1.

$\delta < 0$	$w_C = -1$	$\delta > 0$
$w = 1$	$\xrightarrow{-1}$	$w = 0$

The winding number can also be expressed by the following formula:

$$w_C = \oint_C \frac{d\boldsymbol{k}_{2\mathrm{D}}}{2\pi} \cdot \left[\hat{h}_x(\boldsymbol{k}_{2\mathrm{D}})\boldsymbol{\nabla}\hat{h}_y(\boldsymbol{k}_{2\mathrm{D}}) - \hat{h}_y(\boldsymbol{k}_{2\mathrm{D}})\boldsymbol{\nabla}\hat{h}_x(\boldsymbol{k}_{2\mathrm{D}})\right],$$

where $\boldsymbol{k}_{2\mathrm{D}} = (\delta, k)$ and C represents a closed path. If C encloses the Dirac point, $w_C = -1$; otherwise $w_C = 0$.

From Fig. 9, we can also see that, when δ is fixed and k varies from 0 to $2\pi/a$, $\hat{\boldsymbol{h}}(k)$ rotates once counterclockwise for $\delta < 0$, and $\hat{\boldsymbol{h}}(k)$ does not rotate at all for $\delta > 0$. This single figure combines what are shown in Fig. 3. By increasing δ from a negative value, the path $0 \leq k < 2\pi/a$ crosses the Dirac point and the winding number changes (see also Table 1).

A system with topologically stable degeneracy, such as the Dirac point, is called a topological semimetal. The SSH model, viewed as a two-dimensional model, is an example of a topological semimetal. The original one-dimensional SSH model can be regarded as a cross-section at a fixed δ of this two-dimensional model. A cross-section with $\delta < 0$ is a topological insulator, a cross-section with $\delta > 0$ is a trivial insulator, and the cross-section with $\delta = 0$ passing through the Dirac point is a metal. In this way, a topological insulator can be regarded as a cross-section (in the wave-number space) of a topological semimetal.

Graphene

We investigate the edge states of graphene. In this note, graphene refers to a tight-binding model with nearest-neighbor hopping on a honeycomb lattice. There are four typical edge shapes for graphene, as shown in Fig. 11. The edge states for the bearded edge were investigated in Ref. [4], the armchair edge and zigzag edge in Ref. [5], and the twig edge in Ref. [6]. In this note, we derive these edge states following the approach of Ref. [7].

Hamiltonian and Energy Bands

Here, we consider a honeycomb lattice. The primitive translation vectors are $\boldsymbol{a}_1 = a(\sqrt{3}, 3)/2$ and $\boldsymbol{a}_2 = a(-\sqrt{3}, 3)/2$, where a is the bond length. The vectors connecting the nearest-neighbor sites are $\boldsymbol{\delta}_0 = a(0, 1)$, $\boldsymbol{\delta}_1 = a(-\sqrt{3}, -1)/2$, and $\boldsymbol{\delta}_2 = a(\sqrt{3}, -1)/2$. There is some freedom to select the primitive translation vectors. For example, $\boldsymbol{a}_1$ and $\boldsymbol{a}_1 - \boldsymbol{a}_2 = a(\sqrt{3}, 0)$ may be used as the primitive translation vectors. Here, we define vectors $\boldsymbol{a}_i^{(\mu)} \equiv \boldsymbol{\delta}_\mu - \boldsymbol{\delta}_i$. Then, we can see that $\{\boldsymbol{a}_0^{(\mu)}, \boldsymbol{a}_1^{(\mu)}, \boldsymbol{a}_2^{(\mu)}\}$ is a set of the primitive translation vectors and the zero vector $\boldsymbol{a}_0 = (0, 0)$. In particular, $\{\boldsymbol{a}_0^{(0)}, \boldsymbol{a}_1^{(0)}, \boldsymbol{a}_2^{(0)}\} = \{\boldsymbol{a}_0, \boldsymbol{a}_1, \boldsymbol{a}_2\}$.

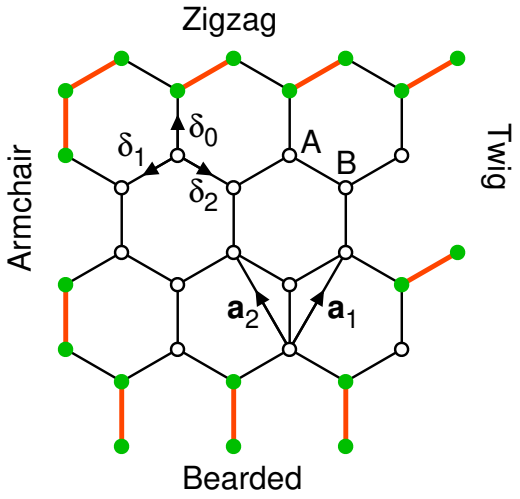

Figure 11: Honeycomb lattice. The primitive translation vectors are $\boldsymbol{a}_1 = a(\sqrt{3}, 3)/2$ and $\boldsymbol{a}_2 = a(-\sqrt{3}, 3)/2$, where a is the bond length. The vectors connecting nearest-neighbor sites are $\boldsymbol{\delta}_0 = a(0, 1)$, $\boldsymbol{\delta}_1 = a(-\sqrt{3}, -1)/2$, and $\boldsymbol{\delta}_2 = a(\sqrt{3}, -1)/2$. Four typical edge shapes are also shown. Each red line connects two sites (green circles), which form a unit cell near an edge.

In a honeycomb lattice, a unit cell contains two sites, and the choice of unit cell is not unique. Here, we choose one μ and take two sites connected by $\boldsymbol{\delta}_\mu$ as a unit cell. A nearest-neighbor site of site $\boldsymbol{r}$ on the A sublattice is site $\boldsymbol{r}+\boldsymbol{\delta}_i = \boldsymbol{r}-\boldsymbol{a}_i^{(\mu)}+\boldsymbol{\delta}_\mu$ on the B sublattice. Then, the Hamiltonian is given by

$$\begin{aligned} H &= t\sum_{\boldsymbol{r}i} c^\dagger_{\boldsymbol{r}A} c_{\boldsymbol{r}-\boldsymbol{a}_i^{(\mu)}B} + \text{h.c.} \\ &= t\sum_{\boldsymbol{k}i} e^{-i\boldsymbol{k}\cdot\boldsymbol{a}_i^{(\mu)}} c^\dagger_{\boldsymbol{k}A} c_{\boldsymbol{k}B} + \text{h.c.} \\ &= \sum_{\boldsymbol{k}} c^\dagger_{\boldsymbol{k}} [h_x^{(\mu)}(\boldsymbol{k})\sigma_x + h_y^{(\mu)}(\boldsymbol{k})\sigma_y] c_{\boldsymbol{k}}, \end{aligned}$$

where,

$$\begin{aligned} h_x^{(\mu)}(\boldsymbol{k}) &= t\sum_i \cos \boldsymbol{k}\cdot\boldsymbol{a}_i^{(\mu)}, \\ h_y^{(\mu)}(\boldsymbol{k}) &= t\sum_i \sin \boldsymbol{k}\cdot\boldsymbol{a}_i^{(\mu)}. \end{aligned}$$

The coefficients $\sum_i e^{-i\boldsymbol{k}\cdot\boldsymbol{a}_i^{(\mu)}}$ that appear in the Hamiltonian depend on the choice of the unit cell. The coefficients for different unit cells are connected by a "gauge transformation": $\sum_i e^{-i\boldsymbol{k}\cdot\boldsymbol{a}_i^{(\nu)}} = e^{i\boldsymbol{k}\cdot\boldsymbol{a}_\nu^{(\mu)}} \sum_i e^{-i\boldsymbol{k}\cdot\boldsymbol{a}_i^{(\mu)}}$.

The single-particle energies are $\pm h(\boldsymbol{k}) = \pm|\boldsymbol{h}^{(\mu)}(\boldsymbol{k})|$ as in the SSH model. It does not depend on μ due to the gauge transformation mentioned above. The energy bands are shown in Fig. 12. The K point, where the upper and lower bands touch, is a Dirac point. Thus, graphene is a topological semimetal.

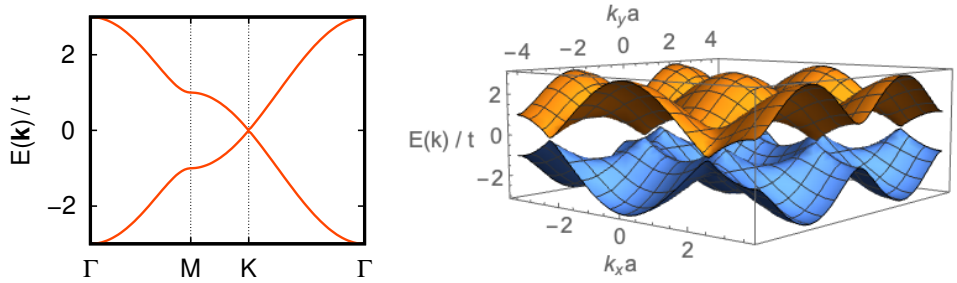

Figure 12: Band structure of graphene. Left panel: on the high symmetry lines. Here, $\Gamma = (0,0)$, $M = 2\pi(0,1/3)/a$, and $K = 2\pi(1/3\sqrt{3}, 1/3)/a$. Right panel: in the entire wave-number space. This figure corresponds to Fig. 8 of the SSH model.

Winding Number of the Vector $\boldsymbol{h}(\boldsymbol{k})$

Here, we want to investigate the structure of $\hat{\boldsymbol{h}}^{(\mu)}(\boldsymbol{k}) = \boldsymbol{h}^{(\mu)}(\boldsymbol{k})/h(\boldsymbol{k})$, as in the case of the SSH model. However, this vector depends on the choice of unit cell μ. It is important to note that, when considering a system with an edge, it is necessary to choose a unit cell that matches the shape of the edge. Looking at Fig. 11, it is necessary to set $\mu = 0$ when considering an armchair edge or bearded edge, and $\mu = 1$ or $\mu = 2$ when considering a twig edge or zigzag edge.

Therefore, we show $\hat{\boldsymbol{h}}^{(\mu)}(\boldsymbol{k})$ for $\mu = 0$ and $\mu = 1$ in Fig. 13. In these figures, $\tilde{a}_1 = (\sqrt{3}/2)a$ represents the lattice constant along the x direction for a system with fixed k_y, while $\tilde{a}_2 = (3/2)a$ denotes the lattice constant along the y direction for a system with fixed k_x. $\hat{\boldsymbol{h}}(\boldsymbol{k})$ rotates once clockwise along a path encircling $K = 2\pi(1/3\sqrt{3}, 1/3)/a = (\pi/3\tilde{a}_1, \pi/\tilde{a}_2)$, so the winding number of the K point is $w_C = -1$. This winding number does not depend on μ due to the gauge transformation. Similarly, the winding number is $w_C = 1$ for $K' = 2\pi(-1/3\sqrt{3}, 1/3)/a = (-\pi/3\tilde{a}_1, \pi/\tilde{a}_2)$.

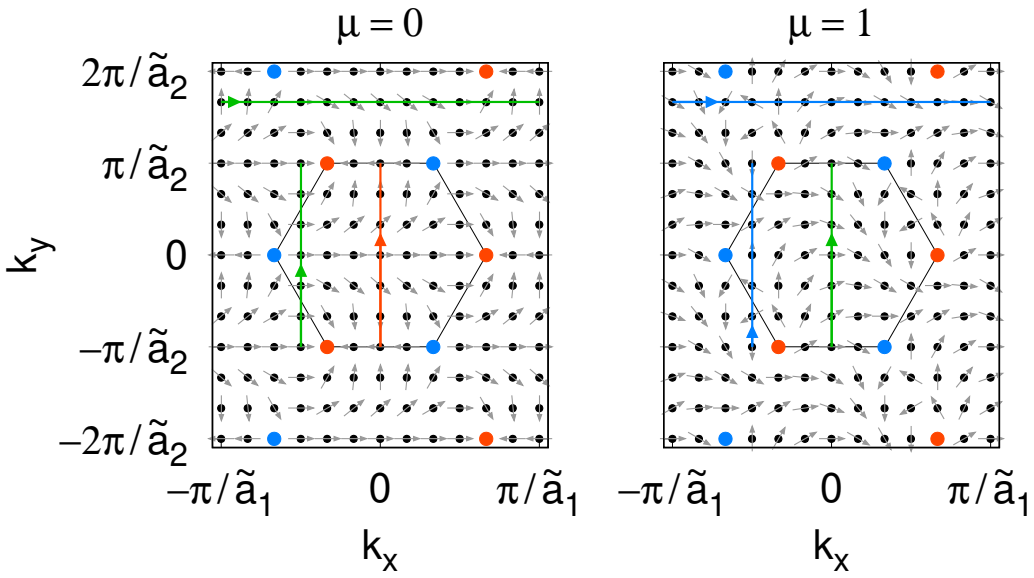

Figure 13: $\hat{\boldsymbol{h}}^{(\mu)}(\boldsymbol{k})$ of graphene. $\mu = 0$ corresponds to a system with armchair or bearded edges, while $\mu = 1$ corresponds to a system with twig or zigzag edges. The region surrounded by the black solid line is the first Brillouin zone. The red points are Dirac points with $w_C = 1$, and the blue points are Dirac points with $w_C = -1$. $\hat{\boldsymbol{h}}(k)$ rotates once counterclockwise along the red path, rotates once clockwise along the blue paths, and does not rotate even once along the green paths. This figure corresponds to Fig. 9 of the SSH model.

First, we consider edges parallel to the y direction, that is, armchair edges or twig edges. In these cases, the wave number k_y can be defined along the y direction. A system with fixed k_y can be regarded as a one-dimensional system along the x direction. It is a cross-section of a topological semimetal. If this one-dimensional system is a topological insulator, edge states should appear for a system with edges. To determine this, we evaluate the winding number $w(k_y)$. By fixing k_y in the $\mu = 0$ figure and varying k_x from $-\pi/\tilde{a}_1$ to $\pi/\tilde{a}_1$, we can obtain the winding number for armchair edges. Similarly, we can obtain the winding number for twig edges from the $\mu = 1$ figure. The same applies to edges parallel to the x direction. By fixing k_x and varying k_y from $-\pi/\tilde{a}_2$ to $\pi/\tilde{a}_2$, we can obtain the winding number for bearded edges from the figure of $\mu = 0$ and for zigzag edges from the figure of $\mu = 1$.

The winding numbers obtained in this way are shown in Fig. 14. The winding number for armchair edges is zero. Conversely, the winding number for twig edges is nonzero in the entire range. The winding number for bearded edges is nonzero in the region where the winding number for zigzag edges is zero, and vice versa. By changing the wave number $k_{\parallel}$ along the edges, the path crosses the Dirac points, and the winding number can change (see also Tables 2 and 3).

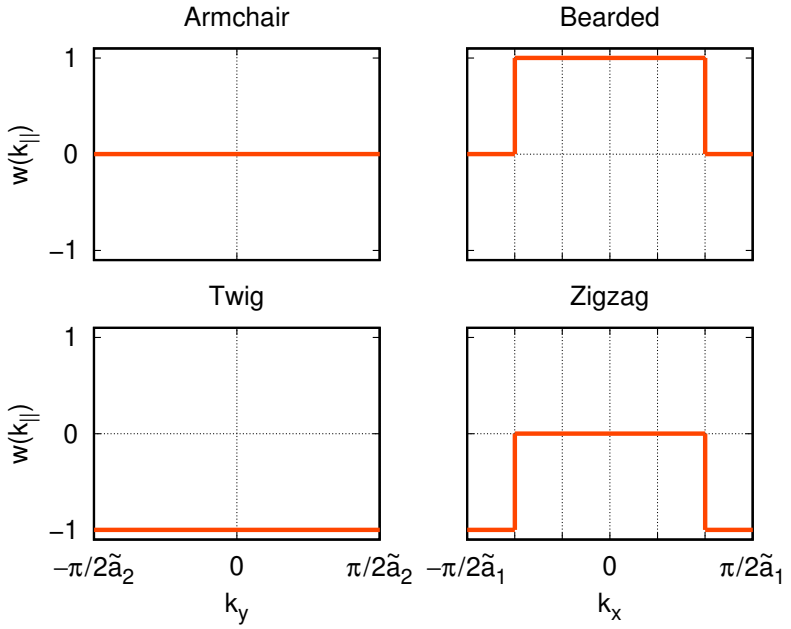

Figure 14: Winding number of graphene. $k_{\parallel}$ is the wave number along the edges: for the armchair edges and twig edges, $k_{\parallel} = k_y$; for the bearded edges and zigzag edges, $k_{\parallel} = k_x$. For the twig edges, the winding number depends on the choice of unit cell; here, we show the case $\mu = 1$. For $\mu = 2$, $w(k_{\parallel}) = 1$.

Table 2: Winding number for the armchair edges ($\mu = 0$) and twig edges ($\mu = 1, 2$). By changing k_y, the path crosses the Dirac points. However, the path simultaneously crosses the Dirac points with $w_C = 1$ and $w_C = -1$, and the winding number $w(k_y)$ does not change. This table corresponds to Table 1 for the SSH model.

	$\frac{\pi}{2\tilde{a}_2} \geq k_y > 0$	$w_C = \pm 1$	$0 > k_y \geq -\frac{\pi}{2\tilde{a}_2}$
$\mu = 0$	$w(k_y) = 0$	$\xrightarrow{+0}$	$w(k_y) = 0$
$\mu = 1$	$w(k_y) = -1$	$\xrightarrow{+0}$	$w(k_y) = -1$
$\mu = 2$	$w(k_y) = 1$	$\xrightarrow{+0}$	$w(k_y) = 1$

Table 3: Winding number for the bearded edges ($\mu = 0$) and zigzag edges ($\mu = 1, 2$). By changing k_x, the path crosses a Dirac point. The change in the winding number $w(k_x)$ depends on the winding number w_C of the Dirac point. This table corresponds to Table 1 for the SSH model.

	$-\frac{\pi}{2\tilde{a}_1} \leq k_x < -\frac{\pi}{3\tilde{a}_1}$	$w_C = 1$	$-\frac{\pi}{3\tilde{a}_1} < k_x < \frac{\pi}{3\tilde{a}_1}$	$w_C = -1$	$\frac{\pi}{3\tilde{a}_1} < k_x \leq \frac{\pi}{2\tilde{a}_1}$
$\mu = 0$	$w(k_x) = 0$	$\xrightarrow{+1}$	$w(k_x) = 1$	$\xrightarrow{-1}$	$w(k_x) = 0$
$\mu = 1, 2$	$w(k_x) = -1$	$\xrightarrow{+1}$	$w(k_x) = 0$	$\xrightarrow{-1}$	$w(k_x) = -1$

Energy Bands of a System with Finite Width

The band structure of graphene with finite width, calculated for each edge shape, is shown in Fig. 15. We can see that zero-energy edge states appear in regions where the winding number is nonzero. This correspondence between the winding number and edge states in graphene was first demonstrated in Ref. [8]. Graphene also has chiral symmetry, as in the SSH model. Therefore, the zero-energy edge states obtained here (doubly degenerate) have amplitudes only on one sublattice on each edge (see Fig. 16).

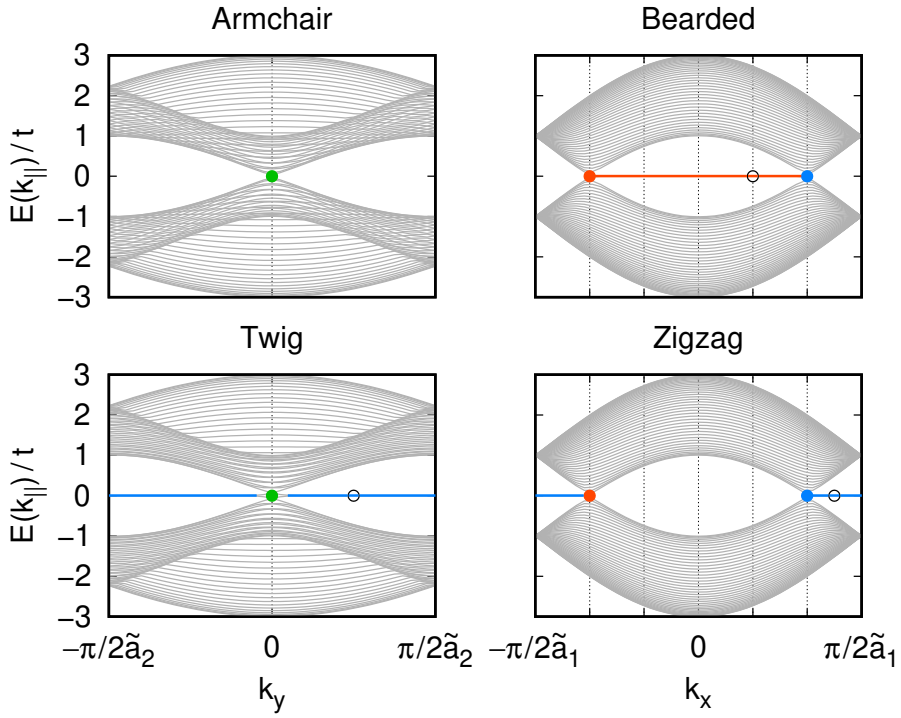

Figure 15: Energy bands of graphene with finite width. The red, blue, and green points are projections of the Dirac points with $w_C = 1$, $w_C = -1$, and $w_C = \pm 1$, respectively. The red line is the zero-energy edge state corresponding to $w = 1$, and the blue lines are the zero-energy edge states corresponding to $w = -1$. For the edge states indicated by the open circles, the charge density is shown in Fig. 16. The present figure corresponds to Fig. 7 of the SSH model.

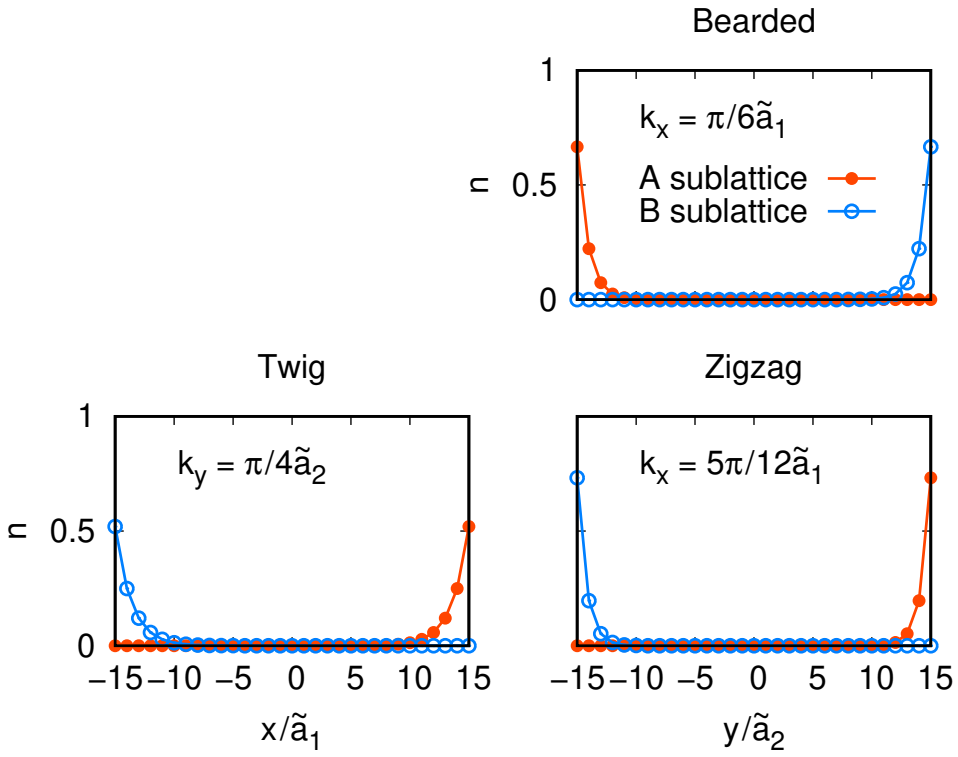

Figure 16: Charge density of the zero-energy edge states of graphene, as indicated by the open circles in Fig. 15. The charge density of the doubly degenerate states has been summed. For twig edges, the result depends on the choice of unit cell; here, we show the case for $\mu = 1$. For $\mu = 2$, the sublattices are interchanged. This figure corresponds to Fig. 6 of the SSH model.

Haldane Model

We have seen that the SSH model and graphene serve as models of one-dimensional topological insulators and two-dimensional topological semimetals. It is due to the existence of point defects of two-component vectors in two dimensions. To extend the models to two-dimensional topological insulators and three-dimensional topological semimetals, we need to consider three-component vectors. This extension of graphene is known as the Haldane model [9].

Hamiltonian and Energy Bands

The Hamiltonian for graphene contains terms proportional to σ_x and σ_y. To make the vector in the Hamiltonian three-component, it is necessary to introduce a term proportional to σ_z. This can be achieved by considering a potential that depends on the sublattice or by including hopping between sites on the same sublattice. Haldane introduced an imaginary hopping integral between the next-nearest-neighbor sites, as shown in Fig. 17.

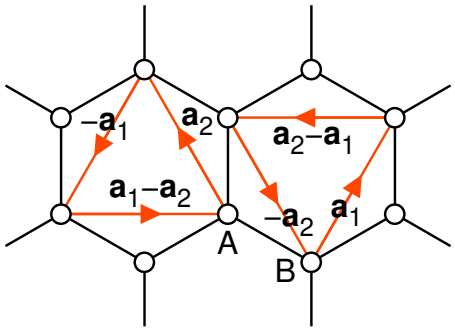

Figure 17: Next-nearest-neighbor hopping in the Haldane model. We assign the hopping integral it_2 to the hopping along the arrows. We assign the hopping integral $-it_2$ to the hopping in the direction opposite to the arrows.

We define vectors connecting the next-nearest-neighbor sites as $\boldsymbol{a}'_0 \equiv \boldsymbol{a}_1 - \boldsymbol{a}_2$, $\boldsymbol{a}'_1 \equiv \boldsymbol{a}_2$, and $\boldsymbol{a}'_2 \equiv -\boldsymbol{a}_1$. The Hamiltonian describing the next-nearest-neighbor hopping is

$$\begin{aligned} H_{\mathrm{nnn}} &= it_2 \sum \left(c^\dagger_{\boldsymbol{r}A} c_{\boldsymbol{r}-\boldsymbol{a}'_i A} + c^\dagger_{\boldsymbol{r}B} c_{\boldsymbol{r}+\boldsymbol{a}'_i B} \right) + \mathrm{h.c.} \\ &= it_2 \sum \left(e^{-i\boldsymbol{k}\cdot\boldsymbol{a}'_i} c^\dagger_{\boldsymbol{k}A} c_{\boldsymbol{k}A} + e^{i\boldsymbol{k}\cdot\boldsymbol{a}'_i} c^\dagger_{\boldsymbol{k}B} c_{\boldsymbol{k}B} \right) + \mathrm{h.c.} \\ &= 2t_2 \sum \sin(\boldsymbol{k}\cdot\boldsymbol{a}'_i)(c^\dagger_{\boldsymbol{k}A} c_{\boldsymbol{k}A} - c^\dagger_{\boldsymbol{k}B} c_{\boldsymbol{k}B}) \\ &= 2t_2 \sum \sin(\boldsymbol{k}\cdot\boldsymbol{a}'_i) c^\dagger_{\boldsymbol{k}} \sigma_z c_{\boldsymbol{k}}. \end{aligned}$$

By including a sublattice-dependent potential, we obtain the coefficient to σ_z as

$$\begin{aligned} h_z(\boldsymbol{k}) &= \Delta + 2t_2 \sum_i \sin(\boldsymbol{k}\cdot\boldsymbol{a}'_i) \\ &= \Delta + 2t_2 \left\{ \sin[\boldsymbol{k}\cdot(\boldsymbol{a}_1 - \boldsymbol{a}_2)] + \sin(\boldsymbol{k}\cdot\boldsymbol{a}_2) - \sin(\boldsymbol{k}\cdot\boldsymbol{a}_1) \right\}. \end{aligned}$$

It does not depend on the choice of unit cell.

The gap closes when $\boldsymbol{h}^{(\mu)}(\boldsymbol{k}) = \left(h_x^{(\mu)}(\boldsymbol{k}), h_y^{(\mu)}(\boldsymbol{k}), h_z(\boldsymbol{k}) \right) = \boldsymbol{0}$. $h_x^{(\mu)}(\boldsymbol{k}) = h_y^{(\mu)}(\boldsymbol{k}) = 0$ at the K and K' points. Therefore, if $h_z(\boldsymbol{k})$ vanishes at these points, the gap closes. Let $K = 2\pi(1/3\sqrt{3}, 1/3)/a = (K_x, K_y)$ and $K' = 2\pi(-1/3\sqrt{3}, 1/3)/a = (K'_x, K'_y)$.

$$\begin{aligned} h_z(K) &= \Delta + 3\sqrt{3}t_2, \\ h_z(K') &= \Delta - 3\sqrt{3}t_2. \end{aligned}$$

Thus, the gap closes at the K point for $\Delta = -3\sqrt{3}t_2$ and at the K' point for $\Delta = 3\sqrt{3}t_2$. The band dispersion is shown in Fig. 18.

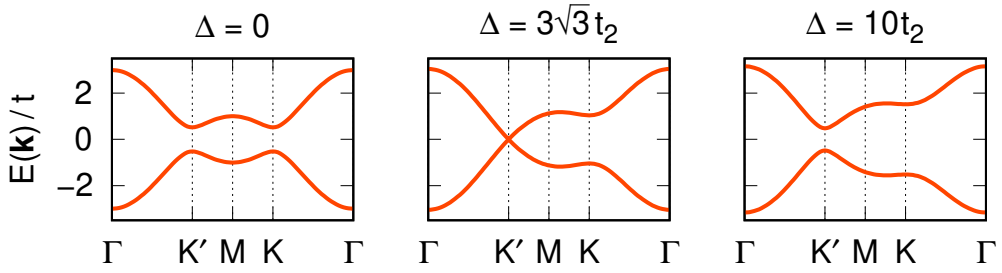

Figure 18: Band dispersion of the Haldane model. $t_2 = 0.1t$. The gap closes at the K' point for $\Delta = 3\sqrt{3}t_2$. This figure corresponds to Fig. 2 of the SSH model.

Winding Number of the Vector $\boldsymbol{h}^{(\mu)}(\boldsymbol{k})$

We consider the normalized three-component vector $\hat{\boldsymbol{h}}^{(\mu)}(\boldsymbol{k}) = \boldsymbol{h}^{(\mu)}(\boldsymbol{k})/|\boldsymbol{h}^{(\mu)}(\boldsymbol{k})|$. The winding number is given by

$$w = \int \frac{dk_x dk_y}{4\pi}\, \hat{\boldsymbol{h}}^{(\mu)}(\boldsymbol{k}) \cdot \frac{\partial \hat{\boldsymbol{h}}^{(\mu)}(\boldsymbol{k})}{\partial k_x} \times \frac{\partial \hat{\boldsymbol{h}}^{(\mu)}(\boldsymbol{k})}{\partial k_y}.$$

This winding number is also called a Chern number. It is obtained by integrating over the first Brillouin zone and does not depend on the choice of unit cell μ. The system is a topological insulator when $w \neq 0$. The winding number as a function of Δ is shown in Fig. 19. There exists a parameter region where $w \neq 0$, and thus, the Haldane model serves as a model for a two-dimensional topological insulator.

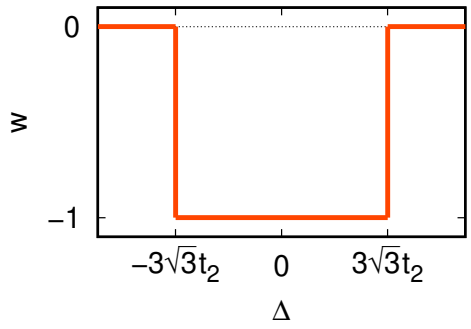

Figure 19: Winding number of the Haldane model. This figure corresponds to Fig. 4 of the SSH model and Fig. 14 of graphene.

Edge States

We show the band structure of systems with edges in Fig. 20. In the case of $\Delta = 2t_2 < 3\sqrt{3}t_2$, the system is a topological insulator with winding number $w = -1$, and edge states emerge that traverse the bulk band gap. In other words, metallic edge states appear, as expected for topological insulators. While details such as the dispersion of the edge states depend on the edge shape, the existence of two edge states and their crossing of the bulk band gap are robust and independent of the specific edge shape. Each edge state is localized on opposite edges and has opposite group velocities. In other words, the state localized on the left edge has a group velocity opposite to that of the state localized on the right edge. Such states are referred to as chiral edge states. In contrast, in the case of $\Delta = 8t_2 > 3\sqrt{3}t_2$, a trivial insulator with $w = 0$, even if edge states appear, they do not traverse the bulk band gap.

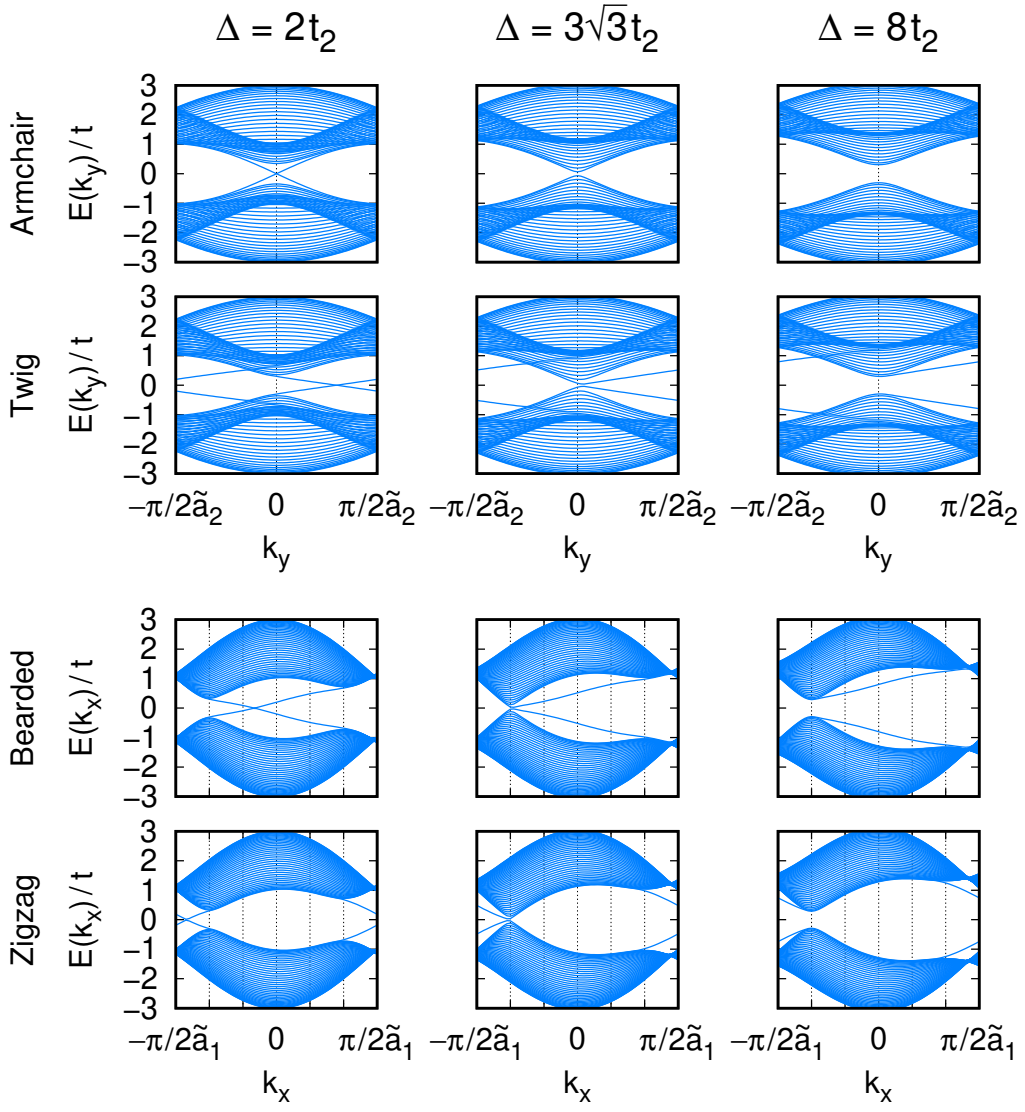

Figure 20: Band structure of the Haldane model with finite widths. $t_2 = 0.1t$. For the twig edges, the band structure depends on the choice of the unit cell. The case of $\mu = 1$ is shown here, while for $\mu = 2$, the corresponding band structure is obtained by inverting k_y. This figure corresponds to Fig. 5 of the SSH model.

Haldane Model as a Three-Dimensional Model

Here, we consider the Haldane model a three-dimensional model by adding Δ to the original two dimensions. We define $\boldsymbol{k}_{3\mathrm{D}} = (k_x, k_y, \Delta)$, and $\boldsymbol{k}_{3\mathrm{D}} = (K_x, K_y, -3\sqrt{3}t_2)$ and $\boldsymbol{k}_{3\mathrm{D}} = (K'_x, K'_y, 3\sqrt{3}t_2)$ are Dirac points. Thus, the Haldane model as a three-dimensional model is a three-dimensional topological semimetal, and its cross-section at a fixed Δ can be a two-dimensional topological insulator.

Winding Number of the Vector $\boldsymbol{h}^{(\mu)}(\boldsymbol{k}_{3\mathrm{D}})$

We consider the normalized three-component vector field $\hat{\boldsymbol{h}}^{(\mu)}(\boldsymbol{k}_{3\mathrm{D}}) = \boldsymbol{h}^{(\mu)}(\boldsymbol{k}_{3\mathrm{D}}) / |\boldsymbol{h}^{(\mu)}(\boldsymbol{k}_{3\mathrm{D}})|$. Let S be a closed surface parametrized by $\boldsymbol{k}_{3\mathrm{D}}(u, v)$. The winding number of $\hat{\boldsymbol{h}}^{(\mu)}(\boldsymbol{k}_{3\mathrm{D}})$ on S is defined as

$$w_S = \int \frac{du\, dv}{4\pi}\, \hat{\boldsymbol{h}}^{(\mu)}(\boldsymbol{k}_{3\mathrm{D}}(u,v)) \cdot \frac{\partial \hat{\boldsymbol{h}}^{(\mu)}(\boldsymbol{k}_{3\mathrm{D}}(u,v))}{\partial u} \times \frac{\partial \hat{\boldsymbol{h}}^{(\mu)}(\boldsymbol{k}_{3\mathrm{D}}(u,v))}{\partial v}.$$

It does not depend on the choice of unit cell μ. The winding number of the Dirac point $\boldsymbol{k}_{3\mathrm{D}} = (K_x, K_y, -3\sqrt{3}t_2)$ is $w_S = -1$, and $w_S = 1$ for $\boldsymbol{k}_{3\mathrm{D}} = (K'_x, K'_y, 3\sqrt{3}t_2)$. We show examples of vector fields with finite winding numbers in Fig. 21. It is known that such a point defect of a three-component vector in three dimensions is topologically stable [3].

The distribution of the Dirac points of the Haldane model in three-dimensional wave-number space is shown in Fig. 22. When the first Brillouin zone crosses a Dirac point by changing Δ, the value of the winding number w changes (see also Table 4).

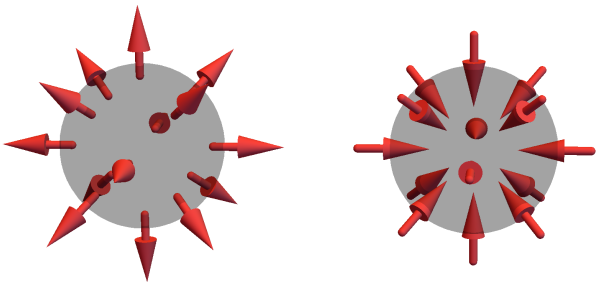

Figure 21: Examples of vector fields with finite winding numbers. Left: $w_S = 1$, Right: $w_S = -1$. This figure corresponds to Fig. 10 for the case of two-component vector fields.

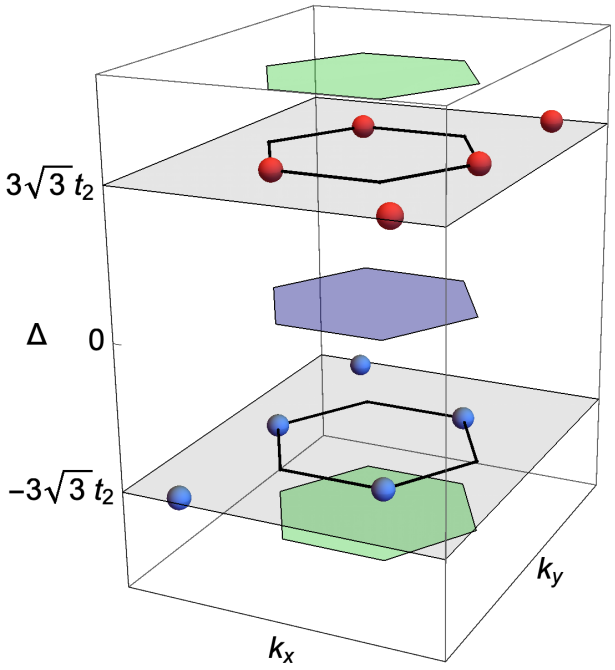

Figure 22: Dirac points of the Haldane model in three-dimensional space. Red points: Dirac points with $w_S = 1$; Blue points: Dirac points with $w_S = -1$. The areas enclosed by the black lines are the first Brillouin zones for $\Delta = \pm 3\sqrt{3}t_2$. The winding number is $w = 0$ for the green regions and $w = -1$ for the blue region. When the first Brillouin zone crosses a Dirac point by changing Δ, the value of the winding number w changes. This figure corresponds to Fig. 9 of the SSH model and Fig. 13 of graphene.

Table 4: Winding number of the Haldane model. When the first Brillouin zone crosses a Dirac point by changing Δ, the value of the winding number w changes depending on the winding number w_S of the Dirac point.

$\Delta < -3\sqrt{3}t_2$	$w_S = -1$	$-3\sqrt{3}t_2 < \Delta < 3\sqrt{3}t_2$	$w_S = 1$	$3\sqrt{3}t_2 < \Delta$
$w = 0$	$\xrightarrow{-1}$	$w = -1$	$\xrightarrow{+1}$	$w = 0$

Fermi Arc

In Fig. 23, we show the minimum absolute value of the single-particle energy, $|E|_{\min}$, for systems with finite widths, plotted on the $k_{\parallel}$-Δ plane. Here, $k_{\parallel}$ is the wave number parallel to the edges. This plane can be regarded as the surface Brillouin zone for the Haldane model treated as a three-dimensional system with surfaces normal to the x or y axis. For a fixed Δ, in the topological insulator phase ($-3\sqrt{3}t_2 < \Delta < 3\sqrt{3}t_2$), edge states traverse the bulk band gap, so that $|E|_{\min} = 0$ at a certain value of $k_{\parallel}$. The line connecting the $|E|_{\min} = 0$ points links the projected points of the Dirac points with $w_S = -1$ and $w_S = 1$. This line is called a Fermi arc [10]. Fermi arcs are a characteristic feature of the surface states of three-dimensional topological semimetals.

In a two-dimensional metal, a line $|E|_{\min} = 0$ appears. It is nothing other than the Fermi surface and appears as a closed loop. In contrast, a Fermi arc appears as an open line, distinguishing it from a Fermi surface.

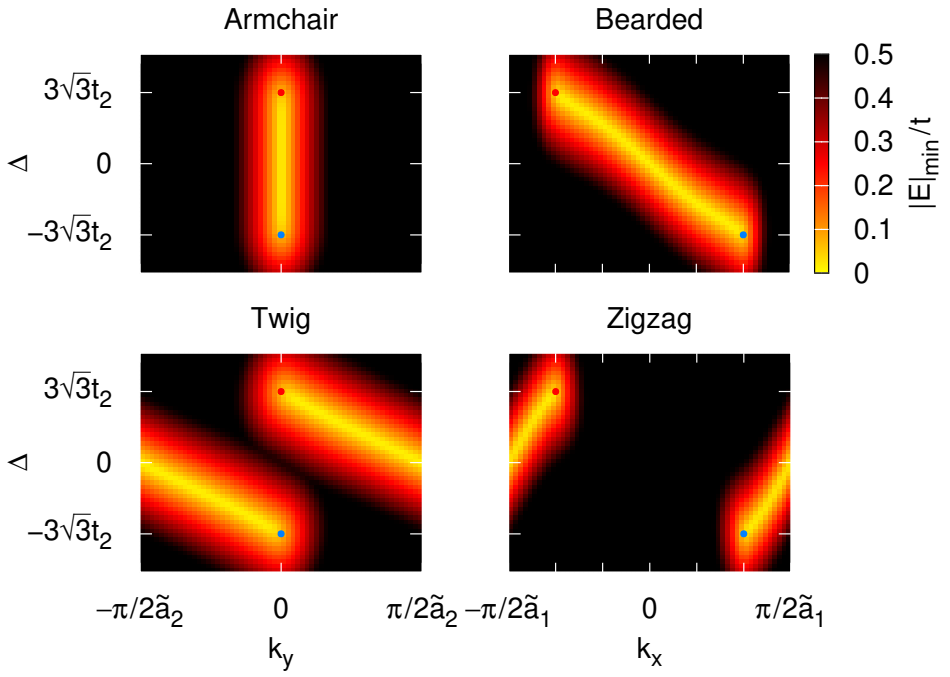

Figure 23: Minimum of the absolute value of the single-particle energy, $|E|_{\min}$, of the Haldane model with finite widths. $t_2 = 0.1t$. It depends on the choice of the unit cell for the twig edges; here, we show the case for $\mu = 1$. For $\mu = 2$, we obtain $|E|_{\min}$ by inverting k_y. Red points: projections of the Dirac points with $w_S = 1$. Blue points: projections of the Dirac points with $w_S = -1$. This figure corresponds to Fig. 7 of the SSH model and Fig. 15 of graphene.

Related Systems

We have investigated the edge states of the SSH model and graphene. In both systems, the edge states originate from point defects of a two-component vector in two dimensions. We have also seen that one-dimensional topological insulators can be regarded as cross-sections of two-dimensional topological semimetals.

A topological semimetal is realized by the degeneracy of the upper and lower bands, so multiple bands are required to realize it. In the SSH model and graphene, a unit cell contains two sites, resulting in two bands. In addition to using the sublattice degrees of freedom, there are other ways to construct two bands. For example, spin degrees of freedom can be employed: spin-orbit coupling can lift the spin degeneracy and split the spin bands. Similarly, orbital degrees of freedom can also be used to realize multiple bands. In fact, studies of edge states arising from similar point defects include investigations of Weyl points and edge states in a two-dimensional Rashba spin-orbit coupling system [11], as well as Dirac points and octupole edge states in a two-dimensional e_g orbital system [12]. These systems have chiral symmetry for specific parameter sets, where the edge states are eigenstates of the chiral operator. Even for general parameters, the edge states retain finite expectation values for this chiral operator.

Also, a line defect of a two-component vector in three-dimensional space is equivalent to a point defect of a two-component vector in two-dimensional space. This is because a two-dimensional cross-section of a three-dimensional space with a line defect has a point defect. As a result, surface states appear in three-dimensional nodal line semimetals [13]. Examples include research on the surface state of a diamond lattice (which has two sublattices like graphene) [7, 14–16] and research on octupole surface states in a three-dimensional e_g orbital system [17]. In particular, the diamond lattice is an extension of graphene investigated in this note to three-dimensional space, and the wave number at which the surface state exists changes depending on the structure of the surface [7]. It is worth noting that rhombohedral graphite, obtained by ABC stacking of graphene, shares the same site connectivity as the diamond lattice with (111) surfaces, leading to the emergence of surface states in a similar way [18].

We have also discussed a three-dimensional topological semimetal and a two-dimensional topological insulator as a cross-section of it, by considering point defects of a three-component vector. The Haldane model employed here has imaginary hopping, which breaks time-reversal symmetry. When we introduce a spin degree of freedom into this model and reverse the sign of the imaginary hopping depending on the spin, the entire system becomes time-reversal symmetric, which is called the Kane-Mele model [19]. This model is known to be characterized by the topological index Z_2 [20].

Table 5 and 6 summarize the systems discussed in this note and this section.

Table 5: Systems with defects in wave-number space. Examples corresponding to cases (1)–(5) are listed in Table 6.

Vector Field	Dimension, Name	Edge or Surface States	
Two-Component	3D Nodal Line Semimetal	Eigenstate of the Chiral Operator	(1)
	2D Topological Semimetal	Eigenstate of the Chiral Operator	(2)
	1D Topological Insulator	Eigenstate of the Chiral Operator	(3)
Three-Component	3D Topological Semimetal	Fermi Arc	(4)
	2D Topological Insulator	Chiral Edge State	(5)

Table 6: Systems with defects in wave-number space: examples for cases (1)–(5) in Table 5.

	Examples	Edge or Surface States
(1)	Diamond Lattice [7, 14–16]	Surface State on a Single Sublattice
	3D e_g Orbital System [17]	Octupole Surface State
(2)	Graphene [4–7]	Edge State on a Single Sublattice
	2D Rashba System [11]	Spin-Polarized Edge State
	2D e_g Orbital System [12]	Octupole Edge State
	SSH Model as a 2D Model	Edge State on a Single Sublattice
(3)	SSH Model [1]	Edge State on a Single Sublattice
	Graphene with Fixed $k_{\parallel}$	Edge State on a Single Sublattice
(4)	Haldane Model as a 3D Model	Fermi Arc
(5)	Haldane Model [9]	Chiral Edge State

References

[1] W. P. Su, J. R. Schrieffer, and A. J. Heeger, Phys. Rev. Lett. **42**, 1698 (1979).

[2] M. Sato, Y. Tanaka, K. Yada, and T. Yokoyama, Phys. Rev. B **83**, 224511 (2011).

[3] M. Nakahara: Geometry, Topology and Physics 2nd Ed. (Taylor & Francis, 2003).

[4] D. J. Klein, Chem. Phys. Lett. **217**, 261 (1994).

[5] M. Fujita, K. Wakabayashi, K. Nakada, and K. Kusakabe, J. Phys. Soc. Jpn. **65**, 1920 (1996).

[6] K. Wakabayashi, S. Okada, R. Tomita, S. Fujimoto, and Y. Natsume, J. Phys. Soc. Jpn. **79**, 034706 (2010).

[7] K. Kubo, J. Phys. Soc. Jpn. **94**, 074701 (2025).

[8] S. Ryu and Y. Hatsugai, Phys. Rev. Lett. **89**, 077002 (2002).

[9] F. D. M. Haldane, Phys. Rev. Lett. **61**, 2015 (1988).

[10] X. Wan, A. M. Turner, A. Vishwanath, and S. Y. Savrasov, Phys. Rev. B **83**, 205101 (2011).

[11] K. Kubo, J. Phys. Soc. Jpn. **93**, 024708 (2024).

[12] K. Kubo, Phys. Rev. B **110**, 075110 (2024).

[13] T. T. Heikkilä and G. E. Volovik, JETP Lett. **93**, 59 (2011).

[14] Y. Takagi and S. Okada, Surf. Sci. **602**, 2876 (2008).

[15] R. Takahashi and S. Murakami, Phys. Rev. B **88**, 235303 (2013).

[16] D. S. Hirashima, J. Phys. Soc. Jpn. **85**, 044705 (2016).

[17] K. Kubo, J. Phys. Soc. Jpn. **94**, 054703 (2025).

[18] M. Koshino, Phys. Rev. B **81**, 125304 (2010).

[19] C. L. Kane and E. J. Mele, Phys. Rev. Lett. **95**, 226801 (2005).

[20] C. L. Kane and E. J. Mele, Phys. Rev. Lett. **95**, 146802 (2005).